# Luminescence and Electron Dynamics in Atomically Precise Nanoclusters with 8 Superatomic Electrons

K. L. Dimuthu M. Weerawardene,<sup>a</sup> Pratima Pandeya,<sup>a</sup> Meng Zhou,<sup>b</sup> Yuxiang Chen,<sup>b</sup> Rongchao Jin,<sup>b</sup> Christine M. Aikens,<sup>a\*</sup>

- a) Department of Chemistry, Kansas State University, Manhattan, KS 66506, USA
- b) Department of Chemistry, Carnegie Mellon University, Pittsburgh, PA 15213, USA \* cmaikens@ksu.edu: 1-785-532-0954

### Abstract

 $[Au_{13}(dppe)_5Cl_2]^{3+}$  $[Au_{25}(SR)_{18}]^{-}$ and The (dppe 1,2bis(diphenylphosphino)ethane) nanoclusters both possess a 13-atom icosahedral core with eight (8e) delocalized superatomic electrons, but their emission properties and timeresolved electron dynamics differ significantly. In this work, experimental photoluminescence and photoluminescence decay measurements are combined with timedependent density functional theory calculations of radiative and non-radiative decay properties and lifetimes to elucidate the similarities and differences in the emission of these two nanoclusters with similar cores. In this work, the photodynamic properties of [Au<sub>13</sub>(dppe)<sub>5</sub>Cl<sub>2</sub>]<sup>3+</sup> are elucidated theoretically for the first time. [Au<sub>13</sub>(dppe)<sub>5</sub>Cl<sub>2</sub>]<sup>3+</sup> exhibits a single strong emission peak compared to the weaker bimodal luminescence of  $[Au_{25}(SR)_{18}]^-$  (modeled here as  $[Au_{25}(SH)_{18}]^-$ ). The strongly emissive state is found to arise from deexcitation out of the  $S_1$  state, similar to  $[Au_{25}(SH)_{18}]^-$ . Both theory and experiment exhibit microsecond lifetimes for this state. Transient absorption measurements and theoretical calculations demonstrate that the excited state lifetimes for higher excited states are typically less than 1 ps. The decay times for the higher excited states of  $[Au_{13}(dppe)_5Cl_2]^{3+}$  and its model compound  $[Au_{13}(pe)_5Cl_2]^{3+}$  (pe = 1,2bis(phosphino)ethane) are observed to be shorter than the lifetimes of the corresponding states of  $[Au_{25}(SR)_{18}]^-$ ; this occurs because the energy gap separating degenerate sets of unoccupied orbitals is only ~0.2 eV in  $[Au_{13}(dppe)_5Cl_2]^{3+}$  compared to a ~0.6 eV energy gap in  $[Au_{25}(SH)_{18}]^-$ .

## Introduction

Subnanometer-sized, ligand-protected gold nanoclusters (AuNCs) are of great interest due to their potential applications in biomedicine, 1-4 catalysis, 5-10 energy conversion, 11-12 etc. Unlike in larger plasmonic gold nanoparticles, quantum size effects dominate the physical and chemical properties of AuNCs in this size regime. These atomically precise AuNCs have discrete electronic states and molecular-like optical properties and are perfect models to elucidate structure-property relationships. They typically consist of a common structural picture: highly symmetrical inorganic cores that follow electronic or geometric closing rules and a layer of ligands to protect the core. A variety of ligands have been used to synthesize AuNCs such as thiolates, <sup>13-35</sup> selenolates, <sup>36-</sup> <sup>39</sup> phosphines, <sup>40-50</sup> alkynyls, <sup>51-56</sup> and mixed ligands. <sup>44-45, 50, 57-62</sup> X-ray crystal structure determinations reveal that thiolate ligands form complex gold-thiolate staple motifs in varying lengths 13-15, 21-25, 29-32 and bind to the gold core through terminal -S groups. Since Au atoms are incorporated in the ligand layer, the gold core in thiolate-protected nanoclusters is generally smaller than the chemical formula of the AuNC implies. For example, the [Au<sub>25</sub>(SR)<sub>18</sub>] cluster (often denoted simply as Au<sub>25</sub>) consists of an icosahedral atom-centered Au@Au<sub>12</sub> core and six v-shaped –(R)S–Au–S(R)–Au–S(R)– staple units that protect 12 surface gold atoms. However in phosphine-protected AuNCs, ligands coordinate to atop sites on the gold core surface forming well-defined ligand layers.

Luminescence properties of AuNCs have been explored extensively during the past couple of decades; near-infrared (NIR) emission energies (0.9-1.8 eV) have been observed regardless of the core size or the identity of the ligand layer, although with a very low quantum efficiency (<0.001).63-67 A majority of studies were focused on the thiolateprotected Au<sub>25</sub> nanocluster and the origin of emission spanning an energy range of 1.1-1.8 eV was attributed to core-based transitions, charge transfer states or ligand-based (semiring) states. 68-75 A recent theoretical investigation by some of us proposes that superatomic P←D transitions, which are Au<sub>13</sub> core-based transitions, are responsible for the emissions in the 1.15-1.55 eV energy region. <sup>76</sup> Moreover, calculations on [Au<sub>25</sub>(SR)<sub>18</sub>]<sup>-</sup> systems ( $R = H, CH_3, C_2H_5, C_3H_7$ ) showed that the ligand/semiring states are not involved but the ligand interactions with the Au<sub>13</sub> core affect the Stokes shifts for longer aliphatic ligands. <sup>76</sup> Higher-energy emission of [Au<sub>25</sub>(SR)<sub>18</sub>] was probed very recently by irradiating at 266 nm and the authors reported that slow electron emission dominates over direct electron detachment, although the energy absorbed (4.66 eV) exceeds the electron detachment threshold energies (2.02-2.36 eV). 77 Recently, Senanayake et al. 78 studied nonradiative relaxation dynamics of the Au<sub>25</sub> nanoparticle theoretically and reported a long relaxation time scale for the first singlet excited state  $(S_1)$  relaxation to the ground state and a much shorter time scale for relaxations between the remainder of the excited states that arise due to  $P \rightarrow D$  transitions. However, it is not yet known whether these photoluminescence and non-radiative relaxation mechanisms for a thiolate-protected gold cluster are applicable to an analogous, phosphine-protected gold cluster.

Herein, we consider the  $[Au_{13}(dppe)_5Cl_2]^{3+}$  cluster (dppe = 1,2-bis(diphenylphosphino)ethane), denoted  $Au_{13}$  for short, which possesses an icosahedral 13-

atom gold core similar to the [Au<sub>25</sub>(SR)<sub>18</sub>] cluster. The x-ray crystal structure of this cluster reveals that 5 bidentate dppe ligands (Figure 1a) protect 10 of the surface gold atoms while two chlorides bind at the two remaining trans positions. 45 This cluster possesses a total charge of +3, which leads to an 8e system and is isoelectronic with the Au<sub>25</sub> system. The chelating effect of the dppe ligand is important to stabilize the Au<sub>13</sub> cluster. This has been emphasized by utilizing other mono- and di-phosphine ligands such as PPh<sub>3</sub>, PMe<sub>2</sub>Ph, POct<sub>3</sub> and PPh<sub>2</sub>-(CH<sub>2</sub>)<sub>m</sub>-PPh<sub>2</sub> (m = 1, 3, 4, 5) during the synthesis procedure. <sup>45, 50</sup> Although geometric and electronic requirements are satisfied to form the stable [Au<sub>13</sub>]<sup>5+</sup> core, the chelating effect of the dppe ligand seems to be significant in the formation of Au<sub>13</sub> clusters. The optical properties of this system have been examined in acetonitrile<sup>45, 50</sup> and the absorption spectrum exhibits three main features around 500, 360, and 300 nm. The spectral profile of the [Au<sub>13</sub>(dppe)<sub>5</sub>Cl<sub>2</sub>]<sup>3+</sup> cluster is qualitatively similar to that of [Au<sub>25</sub>(SR)<sub>18</sub>]<sup>-</sup> cluster<sup>14</sup> in that it displays 3 main absorption peaks. Photoluminescence properties of the Au<sub>13</sub> cluster have also been investigated and a clear band with a quantum yield of 0.062 appearing at 766 nm after excitation at 360 nm has been observed in acetonitrile at room temperature. 45, 50 Very small or negligible emissions have been reported for other phosphine protected gold clusters such as [Au<sub>9</sub>(PPh<sub>3</sub>)<sub>8</sub>]<sup>3+</sup>,<sup>79</sup>  $[Au_{11}(PPh_3)_8Cl_2]^+$ , 80  $[Au_{18}(dppm)_6Cl_4]^{4+}$ , 49 and  $Au_{55}(PPh_3)_{12}Cl_6^{81}$  in solution at room temperature.

In the current study, we compare the ground state and first singlet excited state geometries as well as electronic structures to understand the photoluminescence properties of the chloride and phosphine protected [Au<sub>13</sub>(dppe)<sub>5</sub>Cl<sub>2</sub>]<sup>3+</sup> nanocluster. Theoretical results are compared with experimental emission properties and electron dynamics. Furthermore,

its non-radiative relaxation dynamics around the first main peak of the absorption spectrum are studied using a model cluster where phenyl rings are replaced with hydrogen atoms in the dppe ligand. These results are compared with previous photoluminescence and non-radiative relaxation results of the  $[Au_{25}(SR)_{18}]^-$  cluster.

## **Computational Details**

All geometry optimizations are performed using density functional theory (DFT) as implemented in the Amsterdam Density Functional (ADF) 2017 package.<sup>82</sup> The BP86 exchange-correlation functional<sup>83-84</sup> and full-core double-ζ (DZ) Slater type basis set are used for these calculations. Generalized gradient approximation (GGA) functionals have been employed successfully in calculating geometric and electronic structures as well as optical properties of gold and silver nanoclusters previously. 14, 85-93 All structures are optimized in the gas phase. Well-converged geometries are obtained by tightening the energy and gradient convergence criteria to 1×10<sup>-4</sup> and 1×10<sup>-3</sup> respectively. Scalar relativistic effects are included by utilizing the zeroth-order regular approximation (ZORA). Vertical excitations are calculated at the optimized ground state  $(S_0)$  geometries using time-dependent density functional theory (TDDFT). Finally, the excited state gradients are calculated in order to optimize the excited state geometry. Herein, we calculate the optimized structure for the first singlet excited state (S<sub>1</sub>). Single point TDDFT calculations are performed on the BP86/DZ optimized S<sub>0</sub> and S<sub>1</sub> geometries of [Au<sub>13</sub>(dppe)<sub>5</sub>Cl<sub>2</sub>]<sup>3+</sup> using PBE, <sup>94</sup> B3LYP<sup>95</sup> and PBE0<sup>96-97</sup> functionals and the vertical excitation and emission energies are summarized in Table S1. Continuum solvent calculations using the dielectric constant for acetonitrile are performed using the

conductor-like screening model (COSMO) method.<sup>98</sup> Excited state radiative lifetimes are calculated with the equation<sup>99</sup>

$$\frac{1}{\tau} = \frac{4}{3t_0} \alpha_0^3 (\Delta E)^3 \sum_{\alpha \in (x, y, z)} |M_{\alpha}|^2 \tag{1}$$

where  $\tau$  is the radiative lifetime,  $\alpha_0$  is the fine structure constant,  $\Delta E$  is the excitation energy, and  $M_{\alpha}$  is the transition dipole moment in the  $\alpha=x,y,z$  direction.  $t_0=((4\pi\varepsilon_0)^2\hbar^3/m_e e^4)$  where  $\varepsilon_0$  is the vacuum dielectric constant,  $m_e$  is the mass of the electron, e is the electronic charge and  $\hbar$  is the Planck constant divided by  $2\pi$ .

Nonadiabatic molecular dynamics (NA-MD) simulations are performed with the Vienna Ab initio Simulation Package (VASP)<sup>100</sup> to study the electronic population relaxation dynamics coupled with nuclear degrees of freedom. A temperature ramping calculation is performed on the optimized cluster to thermalize the systems up to 300 K. A simulation box of 24 Å was used to avoid contacts between nanoparticle images. Core electrons are treated using projector-augmented wave (PAW)<sup>101</sup> pseudopotentials while plane wave basis sets are used for valence electrons. A molecular dynamics trajectory of 5 ps is computed using the microcanonical ensemble, Verlet algorithm,<sup>102</sup> and a 1 fs integration time step. Then, a numerical scheme of Tully and Hammes-Schiffer<sup>103</sup> is used to obtain nonadiabatic coupling (NAC) elements along the MD trajectory. Relaxation dynamics are computed using the Fewest Switches Surface Hopping (FSSH) algorithm.<sup>104</sup> Ten different starting geometries are included by splitting the 5 ps MD trajectory into ten sub-trajectories, each of 3.5 ps in length. For each sub-trajectory, 1000 surface hopping trajectories are considered which leads to sufficiently well-converged statistics for the

electronic transitions. Excited state population decay times and ground state population increase times are calculated by fitting to equations 1 and 2 respectively.

$$f(t) = \exp\left(-t \ / \tau\right) \tag{1}$$

$$f(t) = 1 - \exp\left(-t / \tau\right) \tag{2}$$

## **Experimental Details**

The synthesis of [Au<sub>13</sub>(dppe)<sub>5</sub>Cl<sub>2</sub>]<sup>3+</sup> nanoclusters followed the method reported previously. <sup>45</sup> [Au<sub>13</sub>(dppe)<sub>5</sub>Cl<sub>2</sub>]<sup>3+</sup> nanoclusters were dissolved in ethanol to prepare diluted solutions for all spectroscopic measurements. UV-vis absorption spectrum was performed on a Shimadzu UV-3600plus spectrometer. Steady state emission spectrum was measured using a Fluorolog-3 spectrofluorometer from Horiba Jobin Yvon, and time-resolved emission was measured using a time-correlated single photon counting (TCSPC) technique on the same instrument using a pulsed LED source (376 nm, 1.1 ns) as the excitation source. Femtosecond transient absorption (TA) spectra were measured on a commercial Ti:Sapphire laser system. Details of the TA measurements have been described in previous work. <sup>105</sup>

#### Results

#### Geometric and electronic structure

The average bond lengths calculated at the BP86/DZ level of theory for the ground state structure of [Au<sub>13</sub>(dppe)<sub>5</sub>Cl<sub>2</sub>]<sup>3+</sup> in the gas phase are summarized in Table 1 for both the full dppe ligand (Figure 1a) and for a model compound in which the phenyl groups are

replaced with hydrogen atoms to yield the pe-stabilized (pe = 1,2-bis(phosphino)ethane) cluster as depicted in Figure 1b. Reducing the phenyl group on the phosphine groups to H shows minimal to no impact on the average geometrical parameters. However, the individual  $Au_{shell}$ – $Au_{shell}$  bond lengths vary significantly with the pe model ligands (Table S2), and this bond distance has a much higher standard deviation when the model ligands are used. The average  $Au_{center}$ – $Au_{shell}$  and  $Au_{shell}$ – $Au_{shell}$  bond lengths are ~1% shorter than the corresponding bonds of  $[Au_{25}(SH)_{18}]^-$  calculated at the same level of theory. The average  $Au_{shell}$ –Cl bonds are ~6 and ~8% shorter than the average  $Au_{shell}$ –Cl bonds are ~6 and ~8% shorter than the average  $Au_{shell}$ –Cl bonds are ~6 and ~8% shorter than the average  $Au_{shell}$ –Cl bonds are ~6 and ~8% shorter than the average  $Au_{shell}$ –Cl bonds are ~6 and ~8% shorter than the average  $Au_{shell}$ –Cl bonds are ~6 and ~8% shorter than the average  $Au_{shell}$ –Cl bonds are ~6 and ~8% shorter than the average  $Au_{shell}$ –Cl bonds are ~6 and ~8% shorter than the average  $Au_{shell}$ –Cl bonds are ~6 and ~8% shorter than the average  $Au_{shell}$ –Cl bonds are ~6 and ~8% shorter than the average  $Au_{shell}$ –Cl bonds are ~6 and ~8% shorter than the average  $Au_{shell}$ –Cl bonds are ~6 and ~8% shorter than the average  $Au_{shell}$ –Cl bonds are ~6 and ~8% shorter than the average  $Au_{shell}$ –Cl bonds are ~6 and ~8% shorter than the average  $Au_{shell}$ –Cl bonds are ~6 and ~8% shorter than the average  $Au_{shell}$ –Cl bonds are ~6 and ~8% shorter than the average  $Au_{shell}$ –Cl bonds are ~6 and ~8% shorter than the average  $Au_{shell}$ –Cl bonds are ~6 and ~8% shorter than the average  $Au_{shell}$ –Cl bonds are ~6 and ~8% shorter than the average  $Au_{shell}$ –Cl bonds are ~6 and ~8% shorter than  $Au_{shell}$ – $Au_{shell}$ 

**Table 1.** Geometrical parameters of the ground state structure of  $[Au_{13}(dppe)_5Cl_2]^{3+}$  and model  $[Au_{13}(pe)_5Cl_2]^{3+}$  cluster at the BP86/DZ level of theory

	Average Bond Length (Å)		
Bond	$[Au_{13}(pe)_5Cl_2]^{3+}$	$[\mathrm{Au}_{13}(\mathrm{dppe})_5\mathrm{Cl}_2]^{3+}$	
Au <sub>center</sub> —Au <sub>shell</sub>	$2.792 \pm 0.003$	$2.787 \pm 0.014$	
Au <sub>shell</sub> -Au <sub>shell</sub>	$2.938 \pm 0.073$	$2.930 \pm 0.018$	
Au <sub>shell</sub> -P	$2.413 \pm 0.002$	$2.409 \pm 0.003$	
Au <sub>shell</sub> -Cl	$2.365 \pm 0.000$	$2.406 \pm 0.001$	

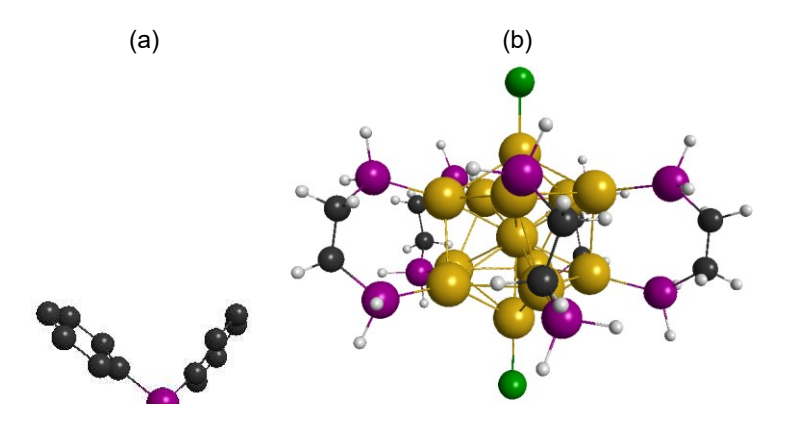


**Figure 1.** The geometric structure of (a) dppe = 1,2-bis(diphenylphosphino)ethane ligand (H atoms are not shown for clarity) and (b)  $[Au_{13}(pe)_5Cl_2]^{3+}$  nanocluster (pe = 1,2-bis(phosphino)ethane) where hydrogen atoms replace the phenyl groups on phosphines. Color code: yellow-Au, purple-P, green-Cl, black-C, white-H

The electronic structure of the  $[Au_{13}(dppe)_5Cl_2]^{3+}$  and  $[Au_{13}(pe)_5Cl_2]^{3+}$  nanoclusters are compared in Figure 2 to identify how the ligand simplification affects the electronic structure of the system. The highest occupied molecular orbital (HOMO) and HOMO-1 are doubly degenerate and exhibit superatomic P character in both clusters whereas the third P orbital lies much lower in energy because the icosahedral symmetry breaks due to the presence of the two axial chlorides. The  $[Au_{13}(dppe)_5Cl_2]^{3+}$  is best described as belonging to the  $D_5$  point group, where the fivefold axis (defined as the z-axis) lies along the axis containing the two chloride ligands. (Due to slight geometrical distortions, calculations are performed with the  $C_1$  point group, but the approximate  $D_5$  symmetry of the nanocluster is evident in its electronic structure.) In consequence, the HOMO and HOMO-1 correspond to an essentially doubly degenerate  $P_x$  and  $P_y$  set, whereas the  $P_z$  orbital (HOMO-2) lies 0.6 eV lower in energy than  $P_x$  and  $P_y$  due to its interaction with atomic p orbitals from the

chloride ligands. In  $[Au_{13}(pe)_5Cl_2]^{3+}$ , the ligand-based (i.e. p atomic orbitals from Cl) and Au d-band orbitals lie closer in energy to the HOMO compared to  $[Au_{13}(dppe)_5Cl_2]^{3+}$ . The  $P_z$  orbital for this system is the HOMO-4, which is only 0.4 eV lower in energy than  $P_x$  and  $P_y$ . In  $[Au_{13}(pe)_5Cl_2]^{3+}$ , HOMO-2 and HOMO-3 primarily arise from Cl p orbitals. By comparing the two nanoclusters, it is also likely that the presence or absence of phenyl groups in the proximity of the Cl ligands may affect the relative energetics of the Cl p orbitals.

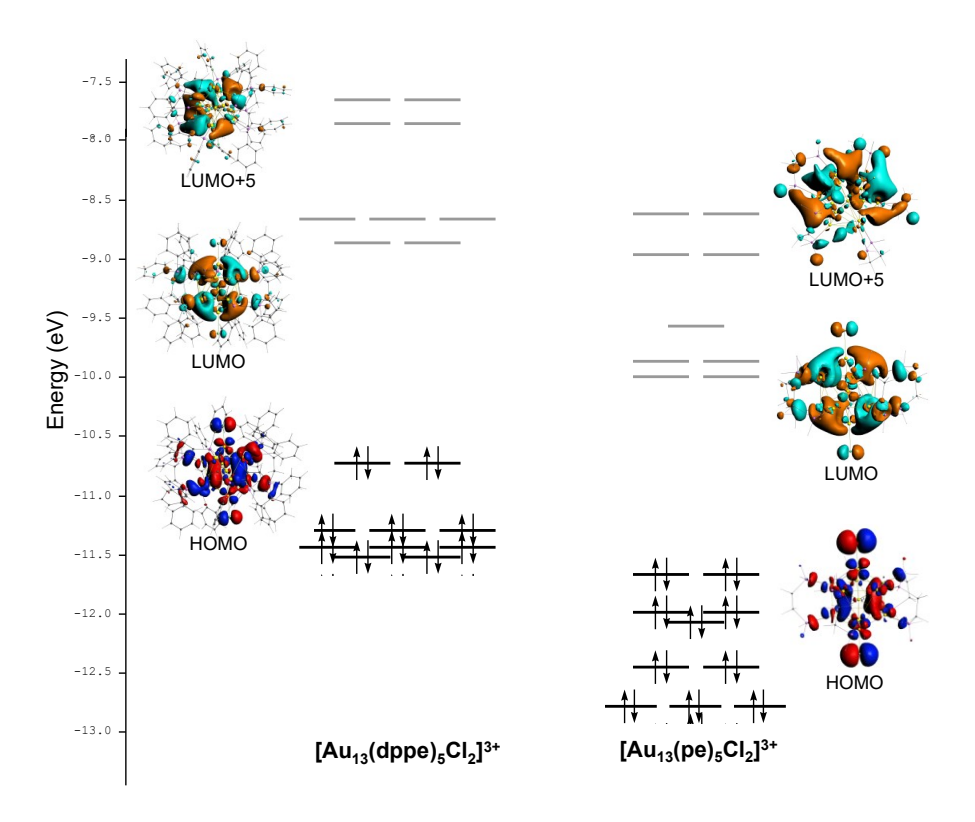


**Figure 2.** Comparison of energy level diagrams and HOMO, LUMO, and LUMO+5 orbitals of [Au<sub>13</sub>(dppe)<sub>5</sub>Cl<sub>2</sub>]<sup>3+</sup> and [Au<sub>13</sub>(pe)<sub>5</sub>Cl<sub>2</sub>]<sup>3+</sup> nanoclusters.

Similar to [Au<sub>25</sub>(SH)<sub>18</sub>]<sup>-</sup>, the lowest unoccupied orbitals in [Au<sub>13</sub>(dppe)<sub>5</sub>Cl<sub>2</sub>]<sup>3+</sup> show superatomic D character and are split into a doubly degenerate and a triply degenerate set.

However the energy gap between these two sets is only  $\sim 0.2$  eV in  $[Au_{13}(dppe)_5Cl_2]^{3+}$  as compared to the ~0.6 eV energy gap in [Au<sub>25</sub>(SH)<sub>18</sub>]<sup>-</sup>. In [Au<sub>13</sub>(dppe)<sub>5</sub>Cl<sub>2</sub>]<sup>3+</sup>, the LUMO and LUMO+1 correspond to the  $D_{xz}$  and  $D_{yz}$  orbital set, the LUMO+2 and LUMO+3 correspond to the  $D_{xy}$  and  $D_{x2-y2}$  set, and the LUMO+4 corresponds to  $D_{z2}$ ; of note, the  $D_{z2}$ orbital is only  $\sim 0.02$  eV higher in energy than the  $D_{xy}$  and  $D_{x2-y2}$  orbitals. [Au<sub>13</sub>(pe)<sub>5</sub>Cl<sub>2</sub>]<sup>3+</sup>, the superatomic D orbitals are split into 3 sets: 2 doubly degenerate sets  $(D_{xz} \text{ and } D_{yz}; D_{xy} \text{ and } D_{x2-y2})$  with a splitting of  $\sim 0.1 \text{ eV}$  and a singly degenerate  $D_{z2}$  orbital that lies ~0.4 eV higher in energy compared to the LUMO. Both clusters have two doubly degenerate sets of superatomic F orbitals with a splitting of ~0.2 eV that lie ~1 eV higher in energy than the LUMO. It is evident that the replacement of phenyl groups on the phosphines by hydrogens has a noteworthy influence on the electronic structure of this system, especially on the splitting between the D orbitals. This effect on electronic structure has previously been observed for other systems such as  $Au_4(PPh_3)_4^{2+}$  and  $Au_4(\mu_2-\mu_3)_4^{2+}$ I)<sub>2</sub>(PPh<sub>3</sub>)<sub>4</sub>, where the presence of  $\pi^*$  orbitals on the phenyl groups was noted to affect excitations in the visible region of the optical absorption spectrum, and thus substitution of PPh<sub>3</sub> with PH<sub>3</sub> could not reproduce the spectrum. <sup>106</sup> This is in contrast to [Au<sub>25</sub>(SR)<sub>18</sub>]<sup>-</sup>, for which substitution of the R groups has relatively minor effects on its absorption spectrum unless the R groups lead to large structural distortions. 107-108

To further explore the ligand effect on the electronic structure of the  $Au_{13}$  system, we performed a constrained optimization by replacing all the phenyl groups by hydrogen atoms and fixing the positions of the Au, Cl, P, and ethyl groups of the  $[Au_{13}(dppe)_5Cl_2]^{3+}$  cluster, allowing only the hydrogen atoms to optimize for  $[Au_{13}(pe)_5Cl_2]^{3+}$ . Figure S1 shows the orbital energy level diagram of this constrained  $[Au_{13}(pe)_5Cl_2]^{3+}$  system. Four

of the superatomic D orbitals are quadruply degenerate and the 5<sup>th</sup> D orbital lies ~0.3 eV higher in energy. The HOMO and HOMO-1 are doubly degenerate superatomic P orbitals and the ligand and *d*-band orbitals lie close in energy to these. Overall, the MO diagram resembles the diagram of fully optimized [Au<sub>13</sub>(pe)<sub>5</sub>Cl<sub>2</sub>]<sup>3+</sup> more than the MO diagram of [Au<sub>13</sub>(dppe)<sub>5</sub>Cl<sub>2</sub>]<sup>3+</sup> shown in Figure 2. These observations imply that the large electronic structure changes are not due to the geometric changes from the simplified ligands, but rather to an electronic effect. In other words, the electronic structure of the phosphine and chloride-protected Au<sub>13</sub> system is considerably ligand-dependent. Therefore, the absorption and luminescence properties are discussed in detail in this work primarily for the [Au<sub>13</sub>(dppe)<sub>5</sub>Cl<sub>2</sub>]<sup>3+</sup> cluster. However, non-radiative relaxation calculations are performed for the [Au<sub>13</sub>(pe)<sub>5</sub>Cl<sub>2</sub>]<sup>3+</sup> cluster due to the required computational resources; this model is expected to be reasonable for these calculations because the density of states are broadened during simulations at finite temperature, and the model ligand provides similar orbitals and orbital ordering with only small effects on the energy gaps.

## *Optical absorption properties*

TDDFT calculations have been performed on the two Au<sub>13</sub> clusters using the BP86/DZ level of theory and their optical absorption spectra are compared in Figure 3. Deviations between the two spectra are expected since their electronic structures are different. As shown in Figure 3(a), the calculated absorption spectrum of the [Au<sub>13</sub>(dppe)<sub>5</sub>Cl<sub>2</sub>]<sup>3+</sup> nanocluster consists of a shoulder peak at 2.07 eV and a prominent peak at 2.16 eV in excellent agreement with the experimental spectrum that exhibits shoulder and prominent peaks at 2.21 and 2.48 eV, respectively. GGA calculations generally

underestimate peak positions<sup>14, 85, 109</sup> of ligand-protected gold and silver nanoclusters, and in this work the underestimation is  $\sim 0.3$  eV for the first peak. Superatomic P to D transitions are found to be responsible for these peaks similar to the first peak of [Au<sub>25</sub>(SR)<sub>18</sub>]<sup>-14</sup> Although the shoulder peak at 2.07 eV and the prominent peak at 2.16 eV are the lowest energy transitions with sufficient oscillator strength to observe experimentally, additional states arising from the P to D transitions are also present in [Au<sub>13</sub>(dppe)<sub>5</sub>Cl<sub>2</sub>]<sup>3+</sup> (see Supporting Information and Table S3 for more information). The experimental spectrum shows two other prominent peaks at 3.44 and 4.13 eV. In comparison, broad peaks centered around 2.95 and 3.66 eV (with multiple shoulder peaks) can be observed in the theoretical spectrum, which are underestimated by  $\sim 0.5$  eV with respect to the experimental spectrum. Analysis of MO→MO transitions involved in these absorption peaks revealed that there are major contributions from orbitals arising from  $Cl_{3p}$  and  $Au_{5d}$  atomic orbitals into superatomic D orbitals as well as superatomic P→F transitions in the 2.95 eV peak. In a perfect icosahedral system, the superatomic P > F transitions would be dipole-forbidden. However, the approximate  $D_5$  symmetry of this nanocluster is greatly reduced compared to the icosahedral symmetry of the core especially because of the two axial chlorides, and additional transitions are allowed. Figure S2 shows that the transition density corresponding to the P $\rightarrow$ F transitions in the 2.95 eV peak is delocalized over the Au<sub>13</sub> core. The peak at 3.66 eV arises mainly due to interband  $Au_{5d} \rightarrow F$  transitions.

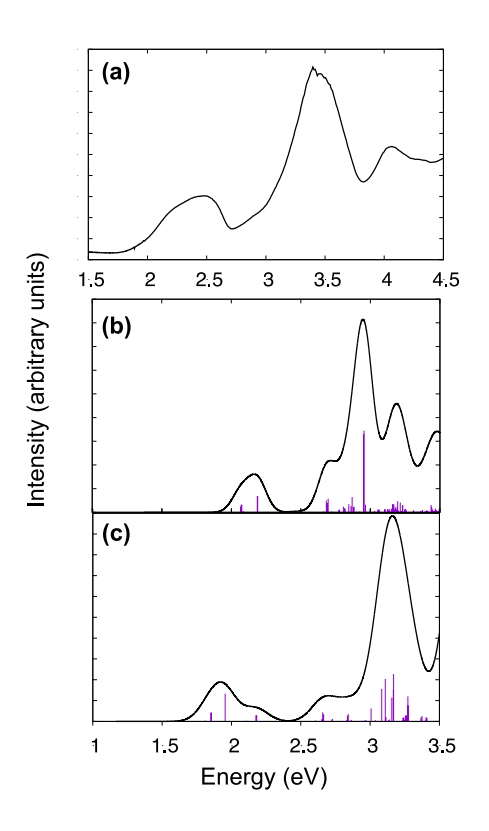


**Figure 3.** (a) Experimental optical absorption spectrum. Calculated spectra of (b)  $[Au_{13}(dppe)_5Cl_2]^{3+}$  nanocluster and (c)  $[Au_{13}(pe)_5Cl_2]^{3+}$  nanocluster at the BP86/DZ level of theory convoluted with a Gaussian with a full width at half-maximum of 0.15 eV.

## Emission properties

To understand the luminescence properties of the  $Au_{13}$  system, we optimized the first singlet excited state  $(S_1)$  of the  $[Au_{13}(dppe)_5Cl_2]^{3+}$  nanocluster. The emission energy is calculated by taking the energy gap between the  $S_0$  and  $S_1$  states at the optimized  $S_1$  geometry. The calculated emission energy of the  $[Au_{13}(dppe)_5Cl_2]^{3+}$  cluster is 1.25 eV and the oscillator strength is two orders of magnitude higher than that of the first excitation at

the ground state geometry. Table 2 encapsulates this information for Au<sub>13</sub> systems and compares the data with that of the isoelectronic Au<sub>25</sub> nanocluster. The experimental photoluminescence (PL) emission spectrum and time-resolved emission decay of [Au<sub>13</sub>(dppe)<sub>5</sub>Cl<sub>2</sub>]<sup>3+</sup> are shown in Figure 4. The PL spectrum is centered at 1.66 eV (Figure 4a), which is comparable to the previous report<sup>50</sup> and agrees well with the theoretical value when the ~0.3 eV underestimation is considered. The calculated emission energy is much smaller than the absorption energy; i.e., the Stokes shift is significant (0.62 eV). The experimental Stokes shift is also large (~0.88 eV) and agrees fairly well with the calculated value. We have also computed the excitation and emission energies using the COSMO continuum solvent model. The excitation and emission energies calculated with TDDFT using a continuum acetonitrile solvent are 1.91 and 1.27 eV, respectively, which are in excellent agreement with the gas phase results of 1.87 and 1.25 eV shown in Table 2. For this nanocluster, inclusion of solvent effects in the calculations does not significantly change the results.

The time-resolved PL probed at 1.66 eV gave a lifetime of 2.2 microseconds (Figure 4b), which is about a factor of 10 shorter than the calculated radiative lifetime (Table 2). Since the time-resolved PL was measured in solution, the experimental PL lifetime could be shortened compared to that in gas phase simulations due to solvation induced non-radiative decay. Tables S2 and S4 report the geometric structural data for the  $S_1$  state of phosphine-protected  $Au_{13}$  systems. The average bond lengths calculated for  $[Au_{13}(dppe)_5Cl_2]^{3+}$  are only  $\sim 0.3\%$  longer than those of the corresponding ground state structure.

**Table 2.** The lowest excitation and emission energies (to/from  $S_1$ ), oscillator strengths, Stokes shifts, and excited state lifetimes for  $[Au_{13}(dppe)_5Cl_2]^{3+}$ ,  $[Au_{13}(pe)_5Cl_2]^{3+}$  and  $[Au_{25}(SR)_{18}]^-$  (Data for  $[Au_{25}(SR)_{18}]^-$  from Ref. 76)

		[Au <sub>13</sub> (dppe) <sub>5</sub> Cl <sub>2</sub> ] <sup>3+</sup>	[Au <sub>13</sub> (pe) <sub>5</sub> Cl <sub>2</sub> ] <sup>3+</sup>	[Au <sub>25</sub> (SH) <sub>18</sub> ] <sup>-</sup>
Excitation	Energy (eV)	1.87	1.67	1.32
	Oscillator	1.05 × 10 <sup>-5</sup>	5.72 × 10 <sup>-6</sup>	4.54 × 10 <sup>-4</sup>
	Strength (au)			
Emission	Energy (eV)	1.25	0.99	0.83
	Oscillator	$6.30 \times 10^{-4}$	5.00 × 10 <sup>-4</sup>	2.46 × 10 <sup>-3</sup>
	Strength (au)	0.30 ^ 10	3.00 ^ 10	2.40 ^ 10
Stokes Shift (eV)		0.62	0.68	0.49
Excited State Lifetime (µs)		23	48	14

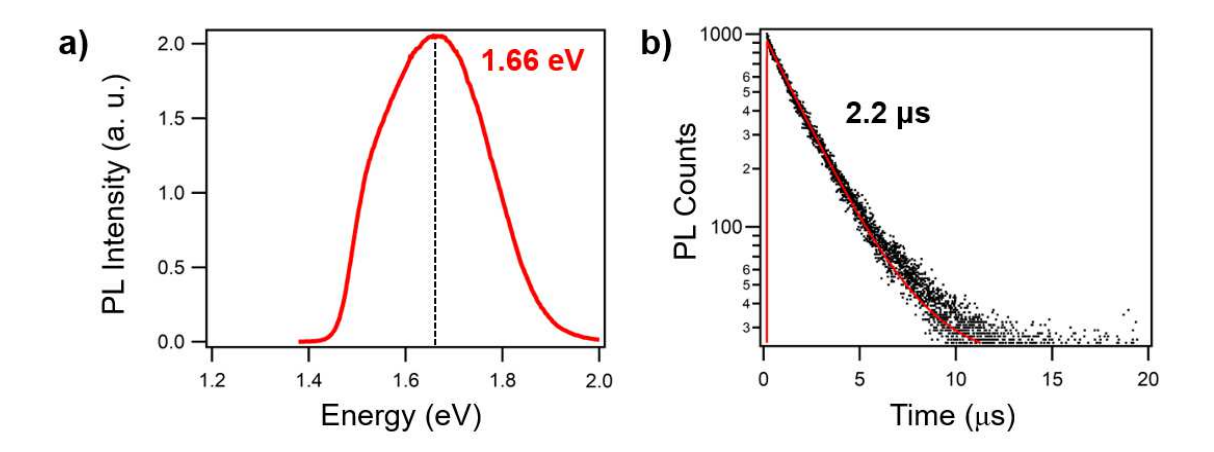


**Figure 4.** (a) Photoluminescence spectrum of [Au<sub>13</sub>(dppe)<sub>5</sub>Cl<sub>2</sub>]<sup>3+</sup> nanoclusters with 2.5 eV excitation; (b) Time-resolved photoluminescence decay probed at 1.66 eV and fit. Data in (a) and (b) are adapted from Ref. 105.

Our previous photoluminescence studies suggest that a large Stokes shift can be associated with noteworthy geometric and electronic structure alterations upon photoexcitation. <sup>76, 110-111</sup> Thus, we examined the individual Au-Au bonds in the Au<sub>13</sub> core of each cluster (Table S2). The [Au<sub>13</sub>(dppe)<sub>5</sub>Cl<sub>2</sub>]<sup>3+</sup> system show a maximum bond elongation of 0.16 Å with lengthening of three other Au<sub>shell</sub>–Au<sub>shell</sub> bonds by ~0.1 Å. Two of the Au<sub>shell</sub>-Au<sub>shell</sub> bonds are shortened by ~0.1 Å as well. These individual bond alterations are smaller compared to the 0.25 Å bond elongations observed with  $[Au_{25}(SH)_{18}]^{-.76}$  In going from the S<sub>0</sub> to the S<sub>1</sub> state, one electron is excited out of the HOMO, which is a superatomic P orbital, and populates the LUMO, which is a superatomic D orbital. The Au<sub>3</sub>-Au<sub>4</sub> and Au<sub>7</sub>-Au<sub>11</sub> bonds that decrease by 0.10 and 0.14 Å in the S<sub>1</sub> geometry lie across the nodal plane of the HOMO, whereas the Au<sub>4</sub>-Au<sub>5</sub> and Au<sub>7</sub>-Au<sub>8</sub> bonds that elongate by 0.16 and 0.13 Å in the  $S_1$  geometry instead lie across a nodal plane of the LUMO as shown in Figure 4. Thus, the excited state bond alterations arise at least in part as a consequence of the bonding/antibonding character of the orbitals involved in the transition.

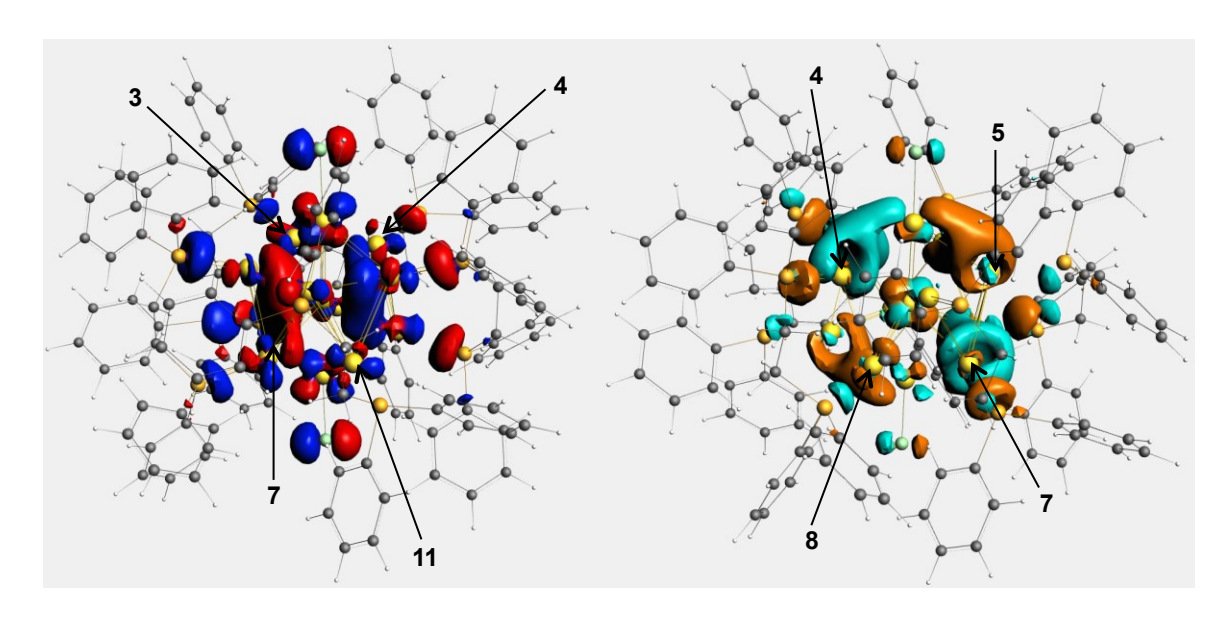


**Figure 5.** The HOMO and LUMO of the  $[Au_{13}(dppe)_5Cl_2]^{3+}$  cluster. The  $Au_3$ - $Au_4$  and  $Au_7$ - $Au_{11}$  bonds shrink and the  $Au_4$ - $Au_5$  and  $Au_7$ - $Au_8$  bonds elongate noticeably upon photoexcitation.

Next, we investigated how the electronic structure transforms upon photoexcitation in the phosphine-protected  $Au_{13}$  cluster. Figure 6 exhibits how the frontier orbitals of  $[Au_{13}(dppe)_5Cl_2]^{3+}$  change in energy as the geometry changes from the  $S_0$  to the  $S_1$  state structure. The initial HOMO and HOMO-1 orbitals are no longer degenerate and the HOMO is destabilized by 0.25 eV in the  $S_1$  state compared to  $S_0$ . Moreover, the LUMO and LUMO+1 orbitals that were also doubly degenerate in the  $S_0$  state are significantly split by 0.50 eV in the  $S_1$  state. This stabilization of the LUMO and destabilization of the HOMO orbitals cause the ground state HOMO-LUMO gap to be reduced by 0.66 eV upon photoexcitation. The nearly triply degenerate, unoccupied, superatomic D orbitals are destabilized by  $\sim 0.1$  eV in the excited state.

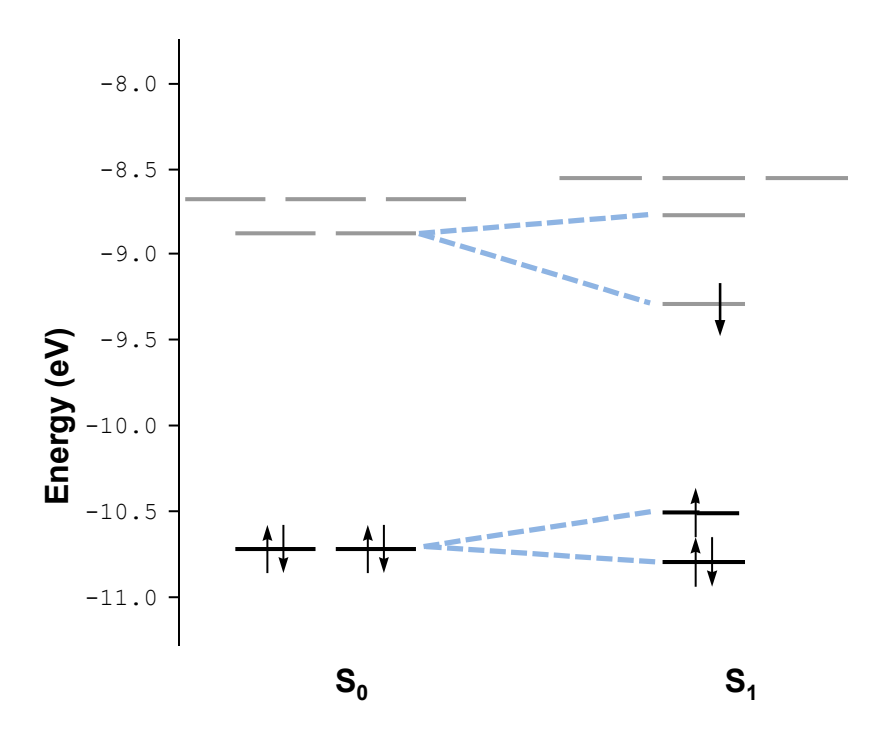


**Figure 6.** Comparison of energy levels of the frontier orbitals in the ground state  $(S_0)$  and excited state  $(S_1)$  of  $[Au_{13}(dppe)_5Cl_2]^{3+}$ . The  $S_1$  state is shown in a cartoon representation with a single electron in one of the D orbitals. Dashed lines are drawn to show the splitting of nearly doubly degenerate HOMO/HOMO-1 and nearly doubly degenerate LUMO/LUMO +1 orbitals of the ground state upon photoexcitation.

The nuclear rearrangements and orbital energy splittings can be considered to arise from a Jahn-Teller effect. In the first excited state, only three electrons populate the  $P_x$  and  $P_y$  orbitals (HOMO-1/HOMO), so a geometrical distortion must occur from the ground state equilibrium geometry so that these orbitals will differ in energy. Similarly, the presence of a single electron in the  $D_{xz}$  and  $D_{yz}$  orbitals (LUMO/LUMO+1) also indicates that a Jahn-Teller distortion must occur. After nuclear relaxation, the  $P_x$  and  $D_{xz}$  orbitals lie lower in energy than the  $P_y$  and  $P_{yz}$  orbitals. In comparison with  $[Au_{25}(SR)_{18}]^-$ , a smaller change in the Au-Au bond distances in  $[Au_{13}(dppe)_5Cl_2]^{3+}$  is associated with a larger

change in the orbital energies, which may be a result of how the P and D orbitals align with the natural axes of the nanoparticle. In  $[Au_{13}(dppe)_5Cl_2]^{3+}$ , orbitals naturally align such that some (the  $P_z$  and  $D_{z2}$  orbitals) lie along the Cl-containing axis; the Jahn-Teller distortion in the  $S_1$  excited state splits the degeneracy of the orbitals in the x and y directions. In contrast in  $[Au_{25}(SR)_{18}]^-$ , the x, y, and z axes are equivalent but the P and D orbitals do not align with the same set of axes. <sup>112</sup>

Even though [Au<sub>13</sub>(pe)<sub>5</sub>Cl<sub>2</sub>]<sup>3+</sup> showed much larger geometric structure modifications upon excited state optimization (Tables S2 and S4), its electronic structure exhibits similar changes as [Au<sub>13</sub>(dppe)<sub>5</sub>Cl<sub>2</sub>]<sup>3+</sup> in the excited state. As demonstrated in Figure S3, the HOMO of [Au<sub>13</sub>(pe)<sub>5</sub>Cl<sub>2</sub>]<sup>3+</sup> is destabilized by 0.19 eV whereas its LUMO is stabilized by 0.52 eV in the S<sub>1</sub> state. Overall, more dramatic orbital splittings are observed for the phosphine-protected gold nanoclusters as compared to our previous studies on thiolate-protected systems.

## *Non-radiative relaxation dynamics*

We studied the first peak at  $\sim$  2 eV and the shoulder peak at  $\sim$  2.8 eV (Figure 3c) to understand the non-radiative electronic relaxation of the lowest energy states in  $[Au_{13}(pe)_5Cl_2]^{3+}$ . The first peak at  $\sim$ 2 eV corresponds to HOMO-4 through LUMO+4 transitions, the shoulder peak at  $\sim$ 2.8 eV arises from HOMO-10 through LUMO+5 transitions, and the second strong peak at 3.2 eV originates from HOMO-14 through LUMO+8 transitions. The orbital energies at 300 K are obtained from the MD simulation (Figure S4). The degeneracies of the orbitals obtained from the optimized geometries

(Figure 2) and from the MD calculation (Figure S4) do not match exactly because the optimizations are performed at 0 K while the MD calculations include the effects of nuclear motion at 300 K. Nonetheless, the HOMO levels are still nearly doubly degenerate. The average HOMO-LUMO gap obtained from the MD simulation is 1.21 eV.

Electronic relaxation dynamics are performed for the states S<sub>1</sub> through S<sub>25</sub>, which correspond to the first absorption peak, to see their relaxation trends and time constants. Excited states for which the non-adiabatic dynamics is performed, along with their respective transitions and decay time constants of excited state populations are listed in Table 3. We also obtained the relaxation dynamics for all 66 states that contribute to the shoulder peak (HOMO-10 through LUMO+5 transitions). Population relaxation for the first 25 states follow the same trends regardless of whether 25 or 66 states are included in the calculation.

**Table 3.** Excited states  $S_1$ - $S_{25}$ , corresponding transitions, and decay times of excited state electronic populations of the  $[Au_{13}(pe)_5Cl_2]^{3+}$  cluster

Excited State	Transition	Decay time (ps)
$S_1$	HOMO → LUMO	20.3
$S_2$	HOMO → LUMO+1	2.0
$S_3$	$HOMO \rightarrow LUMO+2$	1.6
S <sub>4</sub>	$HOMO \rightarrow LUMO+3$	1.3
S <sub>5</sub>	HOMO → LUMO+4	0.9
S <sub>6</sub>	$HOMO-1 \rightarrow LUMO$	2.9
S <sub>7</sub>	HOMO-1 → $LUMO+1$	1.0

$S_8$	HOMO-1 → LUMO+2	1.0
$S_9$	HOMO-1 → $LUMO+3$	0.8
$S_{10}$	HOMO-1 → $LUMO+4$	0.7
$S_{11}$	$HOMO-2 \rightarrow LUMO$	3.6
$S_{12}$	HOMO-2 → LUMO+1	1.2
$S_{13}$	$HOMO-2 \rightarrow LUMO+2$	1.1
$S_{14}$	HOMO-2 → $LUMO+3$	0.8
S <sub>15</sub>	HOMO-2 → $LUMO+4$	0.7
S <sub>16</sub>	$HOMO-3 \rightarrow LUMO$	1.5
S <sub>17</sub>	HOMO-3 → LUMO+1	0.8
$S_{18}$	HOMO-3 → LUMO+2	0.8
S <sub>19</sub>	HOMO-3 → LUMO+3	0.6
$S_{20}$	HOMO-3 → $LUMO+4$	0.6
$S_{21}$	$HOMO-4 \rightarrow LUMO$	1.0
$S_{22}$	HOMO-4 → LUMO+1	0.6
$S_{23}$	HOMO-4 → $LUMO+2$	0.6
S <sub>24</sub>	HOMO-4 → $LUMO+3$	0.5
S <sub>25</sub>	$HOMO-4 \rightarrow LUMO+4$	0.5

The ground state growth times and the decay times are calculated in the presence of all 25 excited states. Decay time constants are in the range of 0.5 ps to 20.3 ps. The

highest decay time occurs for S<sub>1</sub> because of the wide HOMO-LUMO gap; this decay time represents the time required for population in this state to decrease either by relaxation to the ground state (which is slow due to the large HOMO-LUMO gap) or by excitation into a higher excited state (S<sub>2</sub> or above). It should be noted that these NA-MD simulations are less quantitatively accurate for S<sub>1</sub> state decay compared to higher energy states due to the necessity to relax over a large HOMO-LUMO gap. For the other states, decay times are small (0.5-3.6 ps) due to the presence of other nearby intermediate states. The decay time constants obtained for the [Au<sub>13</sub>(pe)<sub>5</sub>Cl<sub>2</sub>]<sup>3+</sup> and the time constants obtained by Senanayake et al.<sup>78</sup> for the Au<sub>25</sub> system are similar, although the S<sub>1</sub> state decay time constant is longer due to the larger HOMO-LUMO gap in the Au<sub>13</sub> system. Both systems have long decay time constant values for the S<sub>1</sub> state compared to other higher excited states.

We further studied the photophysics of [Au<sub>13</sub>(dppe)<sub>5</sub>Cl<sub>2</sub>]<sup>3+</sup> nanoclusters by femtosecond transient absorption (TA) spectroscopy (Figure 7). From the transient absorption data map (pumped at 360 nm), one can observe that the excited state absorption (ESA) band at ~630 nm decays in less than 1 ps to give rise to ESA at around 475 nm (Figure 7a and b), which is similar to the result in our previous study.<sup>105</sup> Between 1 ps and 1.7 ns, there is no significant decay in the TA signal (Figure 7a), which indicates a very long lived excited state lifetime (>>1 ns). Global fitting of the TA data gave two decay components (400 fs and >1 ns). The 400 fs decay component should correspond to the relaxation from higher excited states (with 3.45 eV pump) to the S<sub>1</sub> state. The relaxation times obtained from TA and time-resolved PL measurements agree well with our decay constant values except for S<sub>1</sub>.

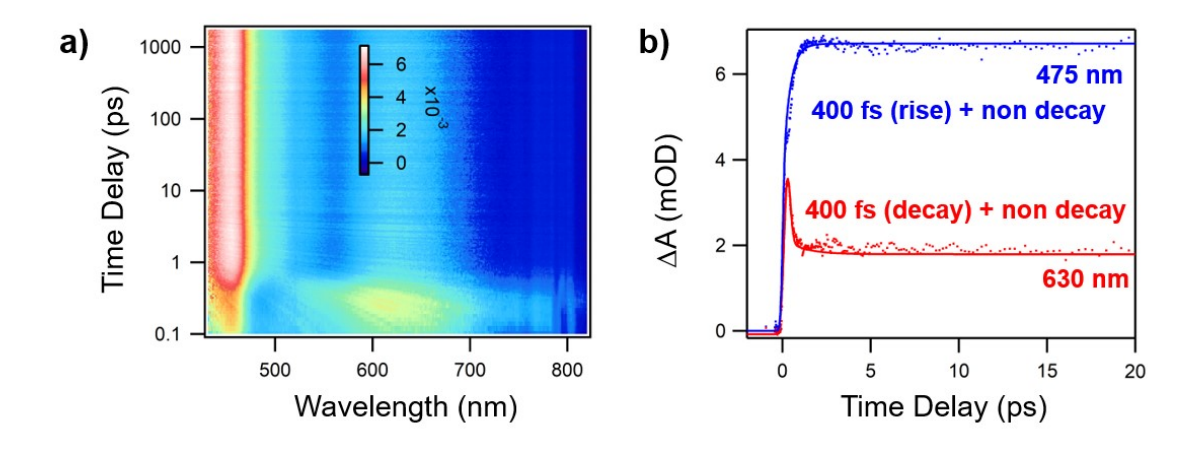


**Figure 7.** (a) Transient absorption (TA) data map with 360 nm (3.45 eV) excitation; (b) TA decay traces and fittings at selected wavelengths.

Excited state population relaxation dynamics of some of the states that correspond to the first absorption peak are shown in Figure 8. It can be observed how the population in each initially excited state relaxes to other state before going to the ground state. For example,  $S_6$  quickly transfers some population to the  $S_1$  state and then a small amount to the  $S_2$  state while the ground state is populated slowly.

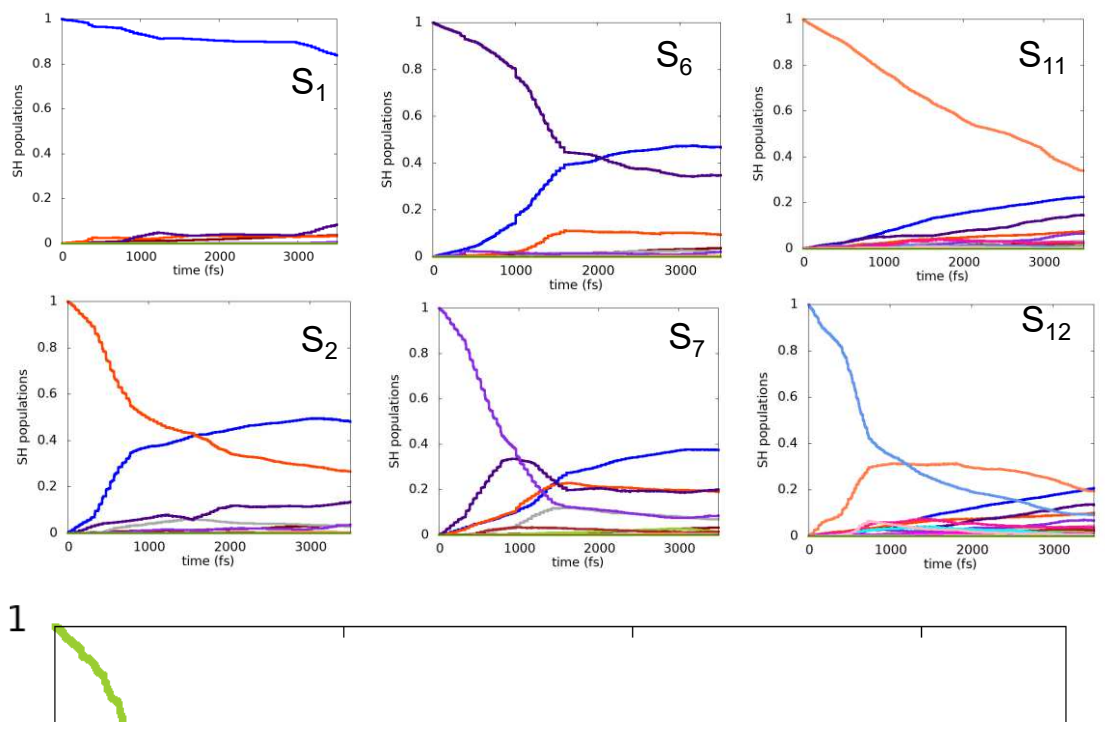


**Figure 8.** Evolution of populations of  $S_1$ ,  $S_2$ ,  $S_6$ ,  $S_7$ ,  $S_{11}$ , and  $S_{12}$  states of  $[Au_{13}(pe)_5Cl_2]^{3+}$  over time

For [Au<sub>13</sub>(pe)<sub>5</sub>Cl<sub>2</sub>]<sup>3+</sup>, the S<sub>11</sub> (HOMO-2 to LUMO) state has a comparatively longer decay time than the decay time of other higher lying states, which could be due to the gap between HOMO-1 and HOMO-2. Similarly, a longer decay time was obtained for the S<sub>7</sub> state (HOMO to LUMO+2) of Au<sub>25</sub> which was also attributed to the large gap between LUMO+1 and LUMO+2. Population relaxation to the intermediate states leads to smaller decay time constant values for the higher energy states. Similarly, the ground state growth times are in the range of 81.6 ps to 375.5 ps (Table S5). Decay times of excited states are faster than the corresponding ground state repopulation times because the electron population moves quickly between the excited states. For example, the decay time for S<sub>1</sub> is 20.3 ps (Table 3) whereas the ground state growth time for the S<sub>1</sub> is 96.9 ps (Table S5)

because the electron population that is initially excited into  $S_1$  can also move into the  $S_2$  and higher states. For states higher than  $S_1$ , the population decay times usually decrease and the ground state repopulation times increase. For example, for  $S_{10}$  the decay time is 0.7 ps while the ground state growth time is 375.5 ps. Ground state repopulation lifetimes (Table S5) are higher for the higher lying states as the population typically relaxes throughout the manifold of intermediate states before falling back to the ground state. The  $Au_{25}$  system also yielded similar trends for the ground state growth times.

#### **Conclusions**

A theoretical investigation has been performed on a phosphine and chloride protected  $Au_{13}$  nanocluster to understand its photoluminescence and non-radiative relaxation properties. Unlike the isoelectronic, thiolate-protected  $[Au_{25}(SH)_{18}]^-$  system, the ligand effect appears to be significant on the electronic structure of the  $Au_{13}$  clusters and hence the optical properties. The lowest emission energy of  $[Au_{13}(dppe)_5Cl_2]^{3+}$  is calculated to be 1.25 eV, which agrees fairly well with the experimental emission  $\sim 1.6$  eV when the theoretical underestimation of  $\sim 0.3$  eV for excitation/emission energies is taken into account. In agreement with experimental results, the photoluminescence lifetime is calculated to be in the microsecond range. A Stokes shift of 0.62 eV is obtained, which is larger than the Stokes shifts calculated for the  $[Au_{25}(SH)_{18}]^-$  systems. Conversely, the geometrical alterations upon photoexcitation are found to be smaller compared to the 0.25 Å bond elongations of  $[Au_{25}(SH)_{18}]^-$ . However, larger electronic structural modifications are observed for  $Au_{13}$  compared to  $Au_{25}$ . Regardless of the differences in ligand layer, the

lowest energy emission of  $Au_{13}$  originates due to superatomic  $P \rightarrow D$  transitions, which are core-based orbitals analogous to those of  $Au_{25}$ .

From the nonradiative relaxation dynamics study, decay time constants for the states that correspond to the first peak were found on the time scale of 0.5 ps to 20.3 ps while the ground state repopulation times were from 81.6 ps to 375.5 ps. The ground state recovery lifetimes are longer for the higher lying states due to the relaxation of population to the intermediate states before relaxing to the ground state. The  $S_1$  state has the longest excited state decay time constant due to the large gap between HOMO and LUMO energy levels. The decay time constants for higher lying states are in good agreement with experiment. The obtained ground state growth times of  $[Au_{13}(pe)_5Cl_2]^{3+}$  are longer than the growth times for the corresponding states of  $Au_{25}$ . In comparison with  $Au_{25}$ , the decay time of  $S_1$  of  $[Au_{13}(pe)_5Cl_2]^{3+}$  is longer due to its larger HOMO-LUMO gap. The decay time for the higher excited states of  $[Au_{13}(pe)_5Cl_2]^{3+}$  are smaller than the lifetimes of the corresponding states of  $Au_{25}$  due to the presence of the excited states close to each other in  $[Au_{13}(pe)_5Cl_2]^{3+}$ .

## **Supporting Information**

Orbital energy level diagram of constrained-optimized  $[Au_{13}(pe)_5Cl_2]^{3+}$  nanocluster by replacing all the phenyl groups by hydrogen atoms; symmetry analysis of the optical absorption spectrum of  $[Au_{13}(dppe)_5Cl_2]^{3+}$ ; transition densities for the 2.98 eV excitation of  $[Au_{13}(dppe)_5Cl_2]^{3+}$ ; comparison of  $Au_{shell}$ — $Au_{shell}$  bond lengths in relaxed geometries of the  $S_0$  and the  $S_1$  state of the  $[Au_{13}(dppe)_5Cl_2]^{3+}$  and  $[Au_{13}(pe)_5Cl_2]^{3+}$  nanoclusters; comparison of energy levels of the frontier orbitals in  $S_0$  and  $S_1$  states of  $[Au_{13}(pe)_5Cl_2]^{3+}$ ; variation of orbital energies of the  $[Au_{13}(pe)_5Cl_2]^{3+}$  cluster with time; excited states, corresponding transitions, and ground state growth times of the  $[Au_{13}(pe)_5Cl_2]^{3+}$  cluster.

## Acknowledgement

This material is based on work supported by the National Science Foundation under Grant No. CHE-1507909. The computing for this project was performed on the Beocat Research Cluster at Kansas State University, which is funded in part by NSF Grants CHE-1726332, CNS-1006860, EPS-1006860, and EPS-0919443.

#### References

- 1. Yang, X.; Yang, M.; Pang, B.; Vara, M.; Xia, Y., Gold Nanomaterials at Work in Biomedicine. *Chem. Rev.* **2015**, *115*, 10410-10488.
- 2. Liu, J.; Yu, M.; Zhou, C.; Yang, S.; Ning, X.; Zheng, J., Passive Tumor Targeting of Renal-Clearable Luminescent Gold Nanoparticles: Long Tumor Retention and Fast Normal Tissue Clearance. *J. Am. Chem. Soc.* **2013**, *135*, 4978-4981.
- 3. Luo, Z.; Zheng, K.; Xie, J., Engineering Ultrasmall Water-Soluble Gold and Silver Nanoclusters for Biomedical Applications. *Chem. Commun.* **2014**, *50*, 5143-5155.
- 4. Chang, W. H.; Lin, C.-A. J.; Lee, C.-H.; Hsieh, J.-T.; Wang, H.-H.; Li, J. K.; Shen, J.-L.; Chan, W.-H.; Yeh, H.-I., Review: Synthesis of Fluorescent Metallic Nanoclusters toward Biomedical Application: Recent Progress and Present Challenges. *J. Med. Biol. Eng.* **2009**, *29*, 276-283.

- 5. Herzing, A. A.; Kiely, C. J.; Carley, A. F.; Landon, P.; Hutchings, G. J., Identification of Active Gold Nanoclusters on Iron Oxide Supports for CO Oxidation. *Science* **2008**, *321*, 1331-1335.
- 6. Turner, M.; Golovko, V. B.; Vaughan, O. P. H.; Abdulkin, P.; Berenguer-Murcia, A.; Tikhov, M. S.; Johnson, B. F. G.; Lambert, R. M., Selective Oxidation with Dioxygen by Gold Nanoparticle Catalysts derived from 55-atom Clusters. *Nature* **2008**, *454*, 981-983.
- 7. Liu, Y.; Tsunoyama, H.; Akita, T.; Xie, S.; Tsukuda, T., Aerobic Oxidation of Cyclohexane Catalyzed by Size-Controlled Au Clusters on Hydroxyapatite: Size Effect in the Sub-2 nm Regime. *ACS Catal.* **2011**, *1*, 2-6.
- 8. Li, G.; Jin, R., Atomically Precise Gold Nanoclusters as New Model Catalysts. *Acc. Chem. Res.* **2013**, *46*, 1749-1758.
- 9. Yamazoe, S.; Koyasu, K.; Tsukuda, T., Nonscalable Oxidation Catalysis of Gold Clusters. *Acc. Chem. Res.* **2014**, *47*, 816-824.
- 10. Higaki, T.; Li, Y.; Zhao, S.; Li, Q.; Li, S.; Du, X.-S.; Yang, S.; Chai, J.; Jin, R., Atomically Tailored Gold Nanoclusters for Catalytic Application. *Angew. Chem. Int. Ed.* 0.
- 11. Chen, Y.-S.; Choi, H.; Kamat, P. V., Metal-Cluster-Sensitized Solar Cells. A New Class of Thiolated Gold Sensitizers Delivering Efficiency Greater than 2%. *J. Am. Chem. Soc.* **2013**, *135*, 8822-8825.
- 12. Abbas, M. A.; Kim, T.-Y.; Lee, S. U.; Kang, Y. S.; Bang, J. H., Exploring Interfacial Events in Gold-Nanocluster-Sensitized Solar Cells: Insights into the Effects of the Cluster Size and Electrolyte on Solar Cell Performance. *J. Am. Chem. Soc.* **2016**, *138*, 390-401.
- 13. Jadzinsky, P. D.; Calero, G.; Ackerson, C. J.; Bushnell, D. A.; Kornberg, R. D., Structure of a Thiol Monolayer-Protected Gold Nanoparticle at 1.1 Å Resolution. *Science* **2007**, *318*, 430-433.
- 14. Zhu, M.; Aikens, C. M.; Hollander, F. J.; Schatz, G. C.; Jin, R., Correlating the Crystal Structure of A Thiol-Protected Au<sub>25</sub> Cluster and Optical Properties. *J. Am. Chem. Soc.* **2008**, *130*, 5883-5885.
- 15. Heaven, M. W.; Dass, A.; White, P. S.; Holt, K. M.; Murray, R. W., Crystal Structure of the Gold Nanoparticle [N(C<sub>8</sub>H<sub>17</sub>)<sub>4</sub>][Au<sub>25</sub>(SCH<sub>2</sub>CH<sub>2</sub>Ph)<sub>18</sub>]. *J. Am. Chem. Soc.* **2008**, *130*, 3754-3755.
- 16. Zhu, M.; Qian, H.; Jin, R., Thiolate-Protected Au<sub>20</sub> Clusters with a Large Energy Gap of 2.1 eV. *J. Am. Chem. Soc.* **2009**, *131*, 7220-7221.
- 17. Zeng, C.; Li, T.; Das, A.; Rosi, N. L.; Jin, R., Chiral Structure of Thiolate-Protected 28-Gold-Atom Nanocluster Determined by X-ray Crystallography. *J. Am. Chem. Soc.* **2013**, *135*, 10011-10013.
- 18. Das, A.; Li, T.; Nobusada, K.; Zeng, C.; Rosi, N. L.; Jin, R., Nonsuperatomic [Au<sub>23</sub>(SC<sub>6</sub>H<sub>11</sub>)<sub>16</sub>] Nanocluster Featuring Bipyramidal Au<sub>15</sub> Kernel and Trimeric Au<sub>3</sub>(SR)<sub>4</sub> Motif. *J. Am. Chem. Soc.* **2013**, *135*, 18264-18267.
- 19. Jiang, D.-e.; Overbury, S. H.; Dai, S., Structure of Au<sub>15</sub>(SR)<sub>13</sub> and Its Implication for the Origin of the Nucleus in Thiolated Gold Nanoclusters. *J. Am. Chem. Soc.* **2013**, *135*, 8786-8789.

- 20. Zeng, C.; Chen, Y.; Li, G.; Jin, R., Synthesis of a Au<sub>44</sub>(SR)<sub>28</sub> Nanocluster: Structure Prediction and Evolution from Au<sub>28</sub>(SR)<sub>20</sub>, Au<sub>36</sub>(SR)<sub>24</sub> to Au<sub>44</sub>(SR)<sub>28</sub>. *Chem. Commun.* **2014**, *50*, 55-57.
- 21. Zeng, C.; Liu, C.; Chen, Y.; Rosi, N. L.; Jin, R., Gold–Thiolate Ring as a Protecting Motif in the Au<sub>20</sub>(SR)<sub>16</sub> Nanocluster and Implications. *J. Am. Chem. Soc.* **2014**, *136*, 11922-11925.
- 22. Das, A.; Liu, C.; Zeng, C.; Li, G.; Li, T.; Rosi, N. L.; Jin, R., Cyclopentanethiolato-Protected Au<sub>36</sub>(SC<sub>5</sub>H<sub>9</sub>)<sub>24</sub> Nanocluster: Crystal Structure and Implications for the Steric and Electronic Effects of Ligand. *J. Phys. Chem. A* **2014**, *118*, 8264-8269.
- 23. Nimmala, P. R.; Knoppe, S.; Jupally, V. R.; Delcamp, J. H.; Aikens, C. M.; Dass, A., Au<sub>36</sub>(SPh)<sub>24</sub> Nanomolecules: X-ray Crystal Structure, Optical Spectroscopy, Electrochemistry, and Theoretical Analysis. *J. Phys. Chem. B* **2014**, *118*, 14157-14167.
- 24. Dass, A.; Theivendran, S.; Nimmala, P. R.; Kumara, C.; Jupally, V. R.; Fortunelli, A.; Sementa, L.; Barcaro, G.; Zuo, X.; Noll, B. C., Au<sub>133</sub>(SPh-*t*Bu)<sub>52</sub> Nanomolecules: X-ray Crystallography, Optical, Electrochemical, and Theoretical Analysis. *J. Am. Chem. Soc.* **2015**, *137*, 4610-4613.
- 25. Das, A.; Liu, C.; Byun, H. Y.; Nobusada, K.; Zhao, S.; Rosi, N.; Jin, R., Structure Determination of [Au<sub>18</sub>(SR)<sub>14</sub>]. *Angew. Chem. Int. Ed.* **2015**, *54*, 3140-3144.
- 26. Yang, H.; Wang, Y.; Edwards, A. J.; Yan, J.; Zheng, N., High-Yield Synthesis and Crystal Structure of a Green Au<sub>30</sub> Cluster Co-Capped by Thiolate and Sulfide. *Chem. Commun.* **2014**, *50*, 14325-14327.
- 27. Yu, Y.; Luo, Z.; Chevrier, D. M.; Leong, D. T.; Zhang, P.; Jiang, D.-e.; Xie, J., Identification of a Highly Luminescent Au<sub>22</sub>(SG)<sub>18</sub> Nanocluster. *J. Am. Chem. Soc.* **2014**, *136*, 1246-1249.
- 28. Chen, Y.; Liu, C.; Tang, Q.; Zeng, C.; Higaki, T.; Das, A.; Jiang, D.-e.; Rosi, N. L.; Jin, R., Isomerism in Au<sub>28</sub>(SR)<sub>20</sub> Nanocluster and Stable Structures. *J. Am. Chem. Soc.* **2016**.
- 29. Crasto, D.; Barcaro, G.; Stener, M.; Sementa, L.; Fortunelli, A.; Dass, A., Au<sub>24</sub>(SAdm)<sub>16</sub> Nanomolecules: X-ray Crystal Structure, Theoretical Analysis, Adaptability of Adamantane Ligands to Form Au<sub>23</sub>(SAdm)<sub>16</sub> and Au<sub>25</sub>(SAdm)<sub>16</sub>, and Its Relation to Au<sub>25</sub>(SR)<sub>18</sub>. J. Am. Chem. Soc. **2014**, 136, 14933-14940.
- 30. Crasto, D.; Malola, S.; Brosofsky, G.; Dass, A.; Häkkinen, H., Single Crystal XRD Structure and Theoretical Analysis of the Chiral Au<sub>30</sub>S(S-*t*-Bu)<sub>18</sub> Cluster. *J. Am. Chem. Soc.* **2014**, *136*, 5000-5005.
- 31. Das, A.; Li, T.; Li, G.; Nobusada, K.; Zeng, C.; Rosi, N. L.; Jin, R., Crystal Structure and Electronic Properties of a Thiolate-protected Au<sub>24</sub> Nanocluster. *Nanoscale* **2014**, *6*, 6458-6462.
- 32. Chen, Y.; Zeng, C.; Liu, C.; Kirschbaum, K.; Gayathri, C.; Gil, R. R.; Rosi, N. L.; Jin, R., Crystal Structure of Barrel-Shaped Chiral Au<sub>130</sub>(p-MBT)<sub>50</sub> Nanocluster. *J. Am. Chem. Soc.* **2015**, *137*, 10076-10079.
- 33. Azubel, M.; Koivisto, J.; Malola, S.; Bushnell, D.; Hura, G. L.; Koh, A. L.; Tsunoyama, H.; Tsukuda, T.; Pettersson, M.; Häkkinen, H.; Kornberg, R. D., Electron Microscopy of Gold Nanoparticles at Atomic Resolution. *Science* **2014**, *345*, 909-912.
- 34. Qian, H.; Eckenhoff, W. T.; Zhu, Y.; Pintauer, T.; Jin, R., Total Structure Determination of Thiolate-Protected Au<sub>38</sub> Nanoparticles. *J. Am. Chem. Soc.* **2010**, *132*, 8280-8281.

- 35. Zeng, C.; Chen, Y.; Kirschbaum, K.; Appavoo, K.; Sfeir, M. Y.; Jin, R., Structural Patterns at All Scales in a Nonmetallic Chiral Au<sub>133</sub>(SR)<sub>52</sub> Nanoparticle. *Sci. Adv.* **2015**, *I*, e1500045.
- 36. Song, Y.; Wang, S.; Zhang, J.; Kang, X.; Chen, S.; Li, P.; Sheng, H.; Zhu, M., Crystal Structure of Selenolate-Protected Au<sub>24</sub>(SeR)<sub>20</sub> Nanocluster. *J. Am. Chem. Soc.* **2014**, *136*, 2963-2965.
- 37. Kurashige, W.; Yamazoe, S.; Kanehira, K.; Tsukuda, T.; Negishi, Y., Selenolate-Protected Au<sub>38</sub> Nanoclusters: Isolation and Structural Characterization. *J. Phys. Chem. Lett.* **2013**, *4*, 3181-3185.
- 38. Xu, Q.; Wang, S.; Liu, Z.; Xu, G.; Meng, X.; Zhu, M., Synthesis of selenolate-protected Au<sub>18</sub>(SeC<sub>6</sub>H<sub>5</sub>)<sub>14</sub> nanoclusters. *Nanoscale* **2013**, *5*, 1176-1182.
- 39. Song, Y.; Cao, T.; Deng, H.; Zhu, X.; Li, P.; Zhu, M., Kinetically Controlled, High-Yield, Direct Synthesis of [Au<sub>25</sub>(SePh)<sub>18</sub>]<sup>-</sup>TOA<sup>+</sup>. *Sci China Chem* **2014**, *57*, 1218-1224.
- 40. Gutiérrez, E.; Powell, R. D.; Furuya, F. R.; Hainfeld, J. F.; Schaaff, T. G.; Shafigullin, M. N.; Stephens, P. W.; Whetten, R. L., Greengold, A Giant Cluster Compound of Unusual Electronic Structure. *Eur. Phys. J. D.* **1999**, *9*, 647-651.
- 41. Chen, J.; Zhang, Q.-F.; Bonaccorso, T. A.; Williard, P. G.; Wang, L.-S., Controlling Gold Nanoclusters by Diphospine Ligands. *J. Am. Chem. Soc.* **2014**, *136*, 92-95.
- 42. Wan, X.-K.; Yuan, S.-F.; Lin, Z.-W.; Wang, Q.-M., A Chiral Gold Nanocluster Au<sub>20</sub> Protected by Tetradentate Phosphine Ligands. *Angew. Chem. Int. Ed.* **2014**, *53*, 2923-2926.
- 43. Chen, J.; Zhang, Q.-F.; Williard, P. G.; Wang, L.-S., Synthesis and Structure Determination of a New Au<sub>20</sub> Nanocluster Protected by Tripodal Tetraphosphine Ligands. *Inorg. Chem.* **2014**, *53*, 3932-3934.
- 44. McKenzie, L. C.; Zaikova, T. O.; Hutchison, J. E., Structurally Similar Triphenylphosphine-Stabilized Undecagolds, Au<sub>11</sub>(PPh<sub>3</sub>)<sub>7</sub>Cl<sub>3</sub> and [Au<sub>11</sub>(PPh<sub>3</sub>)<sub>8</sub>Cl<sub>2</sub>]Cl, Exhibit Distinct Ligand Exchange Pathways with Glutathione. *J. Am. Chem. Soc.* **2014**, *136*, 13426-13435.
- 45. Shichibu, Y.; Konishi, K., HCl-Induced Nuclearity Convergence in Diphosphine-Protected Ultrasmall Gold Clusters: A Novel Synthetic Route to "Magic-Number" Au<sub>13</sub> Clusters. *Small* **2010**, *6*, 1216-1220.
- 46. Shichibu, Y.; Kamei, Y.; Konishi, K., Unique [Core+two] Structure and Optical Property of a Dodeca-Ligated Undecagold Cluster: Critical Contribution of the Exo Gold Atoms to the Electronic Structure. *Chem. Commun.* **2012**, *48*, 7559-7561.
- 47. Zhang, Q.-F.; Williard, P. G.; Wang, L.-S., Polymorphism of Phosphine-Protected Gold Nanoclusters: Synthesis and Characterization of a New 22-Gold-Atom Cluster. *Small* **2016**, *12*, 2518-2525.
- 48. Zhang, S.-S.; Feng, L.; Senanayake, R. D.; Aikens, C. M.; Wang, X.-P.; Zhao, Q.-Q.; Tung, C.-H.; Sun, D., Diphosphine-Protected Ultrasmall Gold Nanoclusters: Opened Icosahedral Au<sub>13</sub> and Heart-Shaped Au<sub>8</sub> Clusters. *Chem. Sci.* **2018**, *9*, 1251-1258.
- 49. Zhang, S.-S.; Senanayake, R. D.; Zhao, Q.-Q.; Su, H.-F.; Aikens, C. M.; Wang, X.-P.; Tung, C.-H.; Sun, D.; Zheng, L.-S., [Au<sub>18</sub>(dppm)<sub>6</sub>Cl<sub>4</sub>]<sup>4+</sup>: A Phosphine-Protected Gold Nanocluster with Rich Charge States. *Dalton Trans.* **2019**, *48*, 3635-3640.
- 50. Shichibu, Y.; Suzuki, K.; Konishi, K., Facile Synthesis and Optical Properties of Magic-Number Au<sub>13</sub> Clusters. *Nanoscale* **2012**, *4*, 4125-4129.

- 51. Wan, X.-K.; Xu, W. W.; Yuan, S.-F.; Gao, Y.; Zeng, X.-C.; Wang, Q.-M., A Near-Infrared-Emissive Alkynyl-Protected Au<sub>24</sub> Nanocluster. *Angew. Chem. Int. Ed.* **2015**, *54*, 9683-9686.
- 52. Wan, X.-K.; Yuan, S.-F.; Tang, Q.; Jiang, D.-e.; Wang, Q.-M., Alkynyl-Protected Au<sub>23</sub> Nanocluster: A 12-Electron System. *Angew. Chem. Int. Ed.* **2015**, *54*, 5977-5980.
- 53. Wan, X.-K.; Tang, Q.; Yuan, S.-F.; Jiang, D.-e.; Wang, Q.-M., Au19 Nanocluster Featuring a V-Shaped Alkynyl–Gold Motif. *J. Am. Chem. Soc.* **2015**, *137*, 652-655.
- 54. Wang, T.; Zhang, W.-H.; Yuan, S.-F.; Guan, Z.-J.; Wang, Q.-M., An Alkynyl-Protected Au<sub>40</sub> Nanocluster Featuring PhC-C–Au–P<sup>^</sup>P Motifs. *Chem. Commun.* **2018**, *54*, 10367-10370.
- Wang, Y.; Wan, X.-K.; Ren, L.; Su, H.; Li, G.; Malola, S.; Lin, S.; Tang, Z.; Häkkinen, H.; Teo, B. K.; Wang, Q.-M.; Zheng, N., Atomically Precise Alkynyl-Protected Metal Nanoclusters as a Model Catalyst: Observation of Promoting Effect of Surface Ligands on Catalysis by Metal Nanoparticles. *J. Am. Chem. Soc.* **2016**, *138*, 3278-3281.
- 56. Lei, Z.; Li, J.-J.; Wan, X.-K.; Zhang, W.-H.; Wang, Q.-M., Isolation and Total Structure Determination of an All-Alkynyl-Protected Gold Nanocluster Au<sub>144</sub>. *Angew. Chem. Int. Ed.* **2018**, *57*, 8639-8643.
- 57. Jin, R.; Liu, C.; Zhao, S.; Das, A.; Xing, H.; Gayathri, C.; Xing, Y.; Rosi, N. L.; Gil, R. R.; Jin, R., Tri-icosahedral Gold Nanocluster [Au<sub>37</sub>(PPh<sub>3</sub>)<sub>10</sub>(SC<sub>2</sub>H<sub>4</sub>Ph)<sub>10</sub>X<sub>2</sub>]<sup>+</sup>: Linear Assembly of Icosahedral Building Blocks. *ACS Nano* **2015**, *9*, 8530-8536.
- 58. Qian, H.; Eckenhoff, W. T.; Bier, M. E.; Pintauer, T.; Jin, R., Crystal Structures of Au<sub>2</sub> Complex and Au<sub>25</sub> Nanocluster and Mechanistic Insight into the Conversion of Polydisperse Nanoparticles into Monodisperse Au<sub>25</sub> Nanoclusters. *Inorg. Chem.* **2011**, *50*, 10735-10739.
- 59. Das, A.; Li, T.; Nobusada, K.; Zeng, Q.; Rosi, N. L.; Jin, R., Total Structure and Optical Properties of a Phosphine/Thiolate-Protected Au<sub>24</sub> Nanocluster. *J. Am. Chem. Soc.* **2012**, *134*, 20286-20289.
- 60. Song, Y.; Fu, F.; Zhang, J.; Chai, J.; Kang, X.; Li, P.; Li, S.; Zhou, H.; Zhu, M., The Magic Au<sub>60</sub> Nanocluster: A New Cluster-Assembled Material with Five Au<sub>13</sub> Building Blocks. *Angew. Chem. Int. Ed.* **2015**, *54*, 8430-8434.
- 61. Wan, X.-K.; Wang, J.-Q.; Nan, Z.-A.; Wang, Q.-M., Ligand Effects in Catalysis by Atomically Precise Gold Nanoclusters. *Science Advances* **2017**, *3*.
- 62. Gutrath, B. S.; Oppel, I. M.; Presly, O.; Beljakov, I.; Meded, V.; Wenzel, W.; Simon, U., [Au<sub>14</sub>(PPh<sub>3</sub>)<sub>8</sub>(NO<sub>3</sub>)<sub>4</sub>]: An Example of a New Class of Au(NO<sub>3</sub>)-Ligated Superatom Complexes. *Angew. Chem. Int. Ed.* **2013**, *52*, 3529-3532.
- 63. Huang, T.; Murray, R. W., Visible Luminescence of Water-Soluble Monolayer-Protected Gold Clusters. *J. Phys. Chem. B* **2001**, *105*, 12498-12502.
- 64. Negishi, Y.; Takasugi, Y.; Sato, S.; Yao, H.; Kimura, K.; Tsukuda, T., Magic-Numbered Au<sub>n</sub> Clusters Protected by Glutathione Monolayers (n = 18, 21, 25, 28, 32, 39): Isolation and Spectroscopic Characterization. *J. Am. Chem. Soc.* **2004**, *126*, 6518-6519.
- 65. Wang, G.; Huang, T.; Murray, R. W.; Menard, L.; Nuzzo, R. G., Near-IR Luminescence of Monolayer-Protected Metal Clusters. *J. Am. Chem. Soc.* **2005**, *127*, 812-813.
- 66. Bigioni, T. P.; Whetten, R. L.; Dag, Ö., Near-Infrared Luminescence from Small Gold Nanocrystals. *J. Phys. Chem. B* **2000**, *104*, 6983-6986.

- 67. Negishi, Y.; Nobusada, K.; Tsukuda, T., Glutathione-Protected Gold Clusters Revisited: Bridging the Gap between Gold(I)—Thiolate Complexes and Thiolate-Protected Gold Nanocrystals. *J. Am. Chem. Soc.* **2005**, *127*, 5261-5270.
- 68. Link, S.; Beeby, A.; FitzGerald, S.; El-Sayed, M. A.; Schaaff, T. G.; Whetten, R. L., Visible to Infrared Luminescence from a 28-Atom Gold Cluster. *J. Phys. Chem. B* **2002**, *106*, 3410-3415.
- 69. Lee, D.; Donkers, R. L.; Wang, G.; Harper, A. S.; Murray, R. W., Electrochemistry and Optical Absorbance and Luminescence of Molecule-like Au<sub>38</sub> Nanoparticles. *J. Am. Chem. Soc.* **2004**, *126*, 6193-6199.
- 70. Shibu, E. S.; Muhammed, M. A. H.; Tsukuda, T.; Pradeep, T., Ligand Exchange of Au<sub>25</sub>SG<sub>18</sub> Leading to Functionalized Gold Clusters: Spectroscopy, Kinetics, and Luminescence. *J. Phys. Chem. C* **2008**, *112*, 12168-12176.
- 71. Shibu, E. S.; Pradeep, T., Photoluminescence and Temperature-Dependent Emission Studies of Au<sub>25</sub> Clusters in the Solid State. *Int. J. Nanosci.* **2009**, *08*, 223-226.
- 72. Wu, Z.; Jin, R., On the Ligand's Role in the Fluorescence of Gold Nanoclusters. *Nano Lett.* **2010**, *10*, 2568-2573.
- 73. Devadas, M. S.; Kim, J.; Sinn, E.; Lee, D.; Goodson, T.; Ramakrishna, G., Unique Ultrafast Visible Luminescence in Monolayer-Protected Au<sub>25</sub> Clusters. *J. Phys. Chem. C* **2010**, *114*, 22417-22423.
- 74. Devadas, M. S.; Bairu, S.; Qian, H.; Sinn, E.; Jin, R.; Ramakrishna, G., Temperature-Dependent Optical Absorption Properties of Monolayer-Protected Au<sub>25</sub> and Au<sub>38</sub> Clusters. *J. Phys. Chem. Lett.* **2011**, *2*, 2752-2758.
- 75. Green, T. D.; Yi, C.; Zeng, C.; Jin, R.; McGill, S.; Knappenberger, K. L., Temperature-Dependent Photoluminescence of Structurally-Precise Quantum-Confined Au<sub>25</sub>(SC<sub>8</sub>H<sub>9</sub>)<sub>18</sub> and Au<sub>38</sub>(SC<sub>12</sub>H<sub>25</sub>)<sub>24</sub> Metal Nanoparticles. *J. Phys. Chem. A* **2014**, *118*, 10611-10621.
- 76. Weerawardene, K. L. D. M.; Aikens, C. M., Theoretical Insights into the Origin of Photoluminescence of Au<sub>25</sub>(SR)<sub>18</sub> Nanoparticles. *J. Am. Chem. Soc.* **2016**, *138*, 11202-11210.
- 77. Hirata, K.; Kim, K.; Nakamura, K.; Kitazawa, H.; Hayashi, S.; Koyasu, K.; Tsukuda, T., Photoinduced Thermionic Emission from  $[M_{25}(SR)_{18}]^-$  (M = Au, Ag) Revealed by Anion Photoelectron Spectroscopy. *J. Phys. Chem. C* **2019**, *123*, 13174-13179.
- 78. Senanayake, R. D.; Akimov, A. V.; Aikens, C. M., Theoretical Investigation of Electron and Nuclear Dynamics in the [Au<sub>25</sub>(SH)<sub>18</sub>]<sup>-1</sup> Thiolate-Protected Gold Nanocluster. *J. Phys. Chem. C* **2017**, *121*, 10653-10662.
- 79. Wen, F.; Englert, U.; Gutrath, B.; Simon, U., Crystal Structure, Electrochemical and Optical Properties of [Au<sub>9</sub>(PPh<sub>3</sub>)<sub>8</sub>](NO<sub>3</sub>)<sub>3</sub>. Eur. J. Inorg. Chem. **2008**, 2008, 106-111.
- 80. Woehrle, G. H.; Warner, M. G.; Hutchison, J. E., Ligand Exchange Reactions Yield Subnanometer, Thiol-Stabilized Gold Particles with Defined Optical Transitions. *J. Phys. Chem. B* **2002**, *106*, 9979-9981.
- 81. Schmid, G.; Pugin, R.; Sawitowski, T.; Simon, U.; Marler, B., Transmission Electron Microscopic and Small Angle X-ray Diffraction Investigations of Au<sub>55</sub>(PPh<sub>3</sub>)<sub>12</sub>Cl<sub>6</sub> Microcrystalst. *Chem. Commun.* **1999**, 1303-1304.

- 82. te Velde, G.; Bickelhaupt, F. M.; Baerends, E. J.; Fonseca Guerra, C.; van Gisbergen, S. J. A.; Snijders, J. G.; Ziegler, T., Chemistry with ADF. *J. Comput. Chem.* **2001**, *22*, 931-967.
- 83. Becke, A. D., Density-Functional Exchange-Energy Approximation with Correct Asymptotic Behavior. *Phys. Rev. A* **1988**, *38*, 3098-3100.
- 84. Perdew, J. P., Density-Functional Approximation For the Correlation Energy of the Inhomogeneous Electron Gas. *Phys. Rev. B* **1986**, *33*, 8822-8824.
- 85. Aikens, C. M., Effects of Core Distances, Solvent, Ligand, and Level of Theory on the TDDFT Optical Absorption Spectrum of the Thiolate-Protected Au<sub>25</sub> Nanoparticle. *J. Phys. Chem. A* **2009**, *113*, 10811-10817.
- 86. Guidez, E. B.; Aikens, C. M., Time-Dependent Density Functional Theory Study of the Luminescence Properties of Gold Phosphine Thiolate Complexes. *J. Phys. Chem. A* **2015**, *119*, 3337-3347.
- 87. Chen, S.; Wang, S.; Zhong, J.; Song, Y.; Zhang, J.; Sheng, H.; Pei, Y.; Zhu, M., The Structure and Optical Properties of the [Au<sub>18</sub>(SR)<sub>14</sub>] Nanocluster. *Angew. Chem. Int. Ed.* **2015,** *54*, 3145-3149.
- 88. Bae, G.-T.; Aikens, C. M., Time-Dependent Density Functional Theory Studies of Optical Properties of Au Nanoparticles: Octahedra, Truncated Octahedra, and Icosahedra. *J. Phys. Chem. C* **2015**, *119*, 23127-23137.
- 89. Hulkko, E.; Lopez-Acevedo, O.; Koivisto, J.; Levi-Kalisman, Y.; Kornberg, R. D.; Pettersson, M.; Häkkinen, H., Electronic and Vibrational Signatures of the Au<sub>102</sub>(p-MBA)<sub>44</sub> Cluster. *J. Am. Chem. Soc.* **2011**, *133*, 3752-3755.
- 90. Liao, M.-S.; Bonifassi, P.; Leszczynski, J.; Ray, P. C.; Huang, M.-J.; Watts, J. D., Structure, Bonding, and Linear Optical Properties of a Series of Silver and Gold Nanorod Clusters: DFT/TDDFT Studies. *J. Phys. Chem. A* **2010**, *114*, 12701-12708.
- 91. Aikens, C. M.; Li, S.; Schatz, G. C., From Discrete Electronic States to Plasmons: TDDFT Optical Absorption Properties of  $Ag_n$  ( $n=10,\,20,\,35,\,56,\,84,\,120$ ) Tetrahedral Clusters. *J. Phys. Chem. C* **2008**, *112*, 11272-11279.
- 92. Malola, S.; Lehtovaara, L.; Häkkinen, H., TDDFT Analysis of Optical Properties of Thiol Monolayer-Protected Gold and Intermetallic Silver–Gold Au<sub>144</sub>(SR)<sub>60</sub> and Au<sub>84</sub>Ag<sub>60</sub>(SR)<sub>60</sub> Clusters. *J. Phys. Chem. C* **2014**, *118*, 20002-20008.
- 93. Juarez-Mosqueda, R.; Malola, S.; Häkkinen, H., Stability, Electronic Structure, and Optical Properties of Protected Gold-Doped Silver  $Ag_{29-x}Au_x$  (x=0-5) Nanoclusters. *Phys. Chem. Phys.* **2017**, *19*, 13868-13874.
- 94. Perdew, J. P.; Burke, K.; Ernzerhof, M., Generalized Gradient Approximation Made Simple. *Phys. Rev. Lett.* **1996,** 77, 3865-3868.
- 95. Stephens, P. J.; Devlin, F. J.; Chabalowski, C. F.; Frisch, M. J., Ab Initio Calculation of Vibrational Absorption and Circular Dichroism Spectra Using Density Functional Force Fields. *J. Phys. Chem.* **1994**, *98*, 11623-11627.
- 96. Grimme, S., Accurate Description of van der Waals Complexes by Density Functional Theory including Empirical Corrections. *J. Comput. Chem.* **2004**, *25*, 1463-1473.
- 97. Ernzerhof, M.; Scuseria, G. E., Assessment of the Perdew–Burke–Ernzerhof Exchange-Correlation Functional. *J. Chem. Phys.* **1999**, *110*, 5029-5036.

- 98. Klamt, A.; Schuurmann, G., COSMO: A New Approach to Dielectric Screening in Solvents with Explicit Expressions for the Screening Energy and its Gradient. *Journal of the Chemical Society, Perkin Transactions 2* **1993**, 799-805.
- 99. Mori, K.; Goumans, T. P. M.; van Lenthe, E.; Wang, F., Predicting Phosphorescent Lifetimes and Zero-Field Splitting of Organometallic Complexes with Time-Dependent Density Functional Theory including Spin-Orbit Coupling. *Phys. Chem. Chem. Phys.* **2014**, *16*, 14523-14530.
- 100. Kresse, G.; Furthmüller, J., Efficiency of Ab-Initio Total Energy Calculations for Metals and Semiconductors using a Plane-Wave Basis Set. *Comput. Mater. Sci.* **1996**, *6*, 15-50.
- 101. Kresse, G.; Joubert, D., From Ultrasoft Pseudopotentials to the Projector Augmented-Wave Method. *Phys. Rev. B* **1999**, *59*, 1758-1775.
- 102. Verlet, L., Computer "Experiments" on Classical Fluids. I. Thermodynamical Properties of Lennard-Jones Molecules. *Phys. Rev.* **1967**, *159*, 98-103.
- 103. Hammes Schiffer, S.; Tully, J. C., Proton Transfer in Solution: Molecular Dynamics with Quantum Transitions. *J. Chem. Phys.* **1994**, *101*, 4657-4667.
- 104. C. Tully, J., Mixed Quantum-Classical Dynamics. *Faraday Discuss.* **1998**, *110*, 407-419.
- 105. Zhou, M.; Jin, R.; Sfeir, M. Y.; Chen, Y.; Song, Y.; Jin, R., Electron Localization in Rod-Shaped Triicosahedral Gold Nanocluster. *Proc. Natl. Acad. Sci. U. S. A.* **2017**, *114*, E4697-E4705.
- 106. Ivanov, S. A.; Arachchige, I.; Aikens, C. M., Density Functional Analysis of Geometries and Electronic Structures of Gold-Phosphine Clusters: The Case of  $Au_4(PR_3)_4^{2+}$  and  $Au_4(\mu_2-I)_2(PR_3)_4$ . *J. Phys. Chem. A* **2011**, *115*, 8017-8031.
- 107. Tlahuice-Flores, A.; Whetten, R. L.; Jose-Yacaman, M., Ligand Effects on the Structure and the Electronic Optical Properties of Anionic Au<sub>25</sub>(SR)<sub>18</sub> Clusters. *J. Phys. Chem. C* **2013**, *117*, 20867-20875.
- 108. Schaaff, T. G.; Whetten, R. L., Giant Gold-Glutathione Cluster Compounds: Intense Optical Activity in Metal-Based Transitions. *J. Phys. Chem. B* **2000**, *104*, 2630-2641.
- 109. Marques, M. A. L.; Castro, A.; Rubio, A., Assessment of Exchange-Correlation Functionals for the Calculation of Dynamical Properties of Small Clusters in Time-Dependent Density Functional Theory. *J. Chem. Phys.* **2001**, *115*, 3006-3014.
- 110. Weerawardene, K. L. D. M.; Guidez, E. B.; Aikens, C. M., Photoluminescence Origin of Au<sub>38</sub>(SR)<sub>24</sub> and Au<sub>22</sub>(SR)<sub>18</sub> Nanoparticles: A Theoretical Perspective. *J. Phys. Chem. C* **2017**, *121*, 15416-15423.
- 111. Weerawardene, K. L. D. M.; Aikens, C. M., Origin of Photoluminescence of Ag<sub>25</sub>(SR)<sub>18</sub> Nanoparticles: Ligand and Doping Effect. *J. Phys. Chem. C* **2018**, *122*, 2440-2447.
- 112. Aikens, C. M., Origin of Discrete Optical Absorption Spectra of  $M_{25}(SH)_{18}^{-1}$  Nanoparticles (M = Au, Ag). *J. Phys. Chem. C* **2008**, *112*, 19797-19800.

## **TOC GRAPHIC**

